Freezing immunoglobulins to see them move

L. Bongini*†, D. Fanelli†‡, F. Piazza†§, P. De Los Rios§, S. Sandin‡, and U. Skoglund‡¶

*Centro Interdipartimentale per lo Studio delle Dinamiche Complesse, Università di Firenze, Via G. Sansone 1, 50019 Florence, Italy; ‡Cell and Molecular Biology Department, Karolinska Institutet, 171 77 Stockholm, Sweden; and §Institute de Physique Théorique, École Polytechnique Fédérale de Lausanne, BP CH-1015, Lausanne, Switzerland

Edited by Roger D. Kornberg, Stanford University School of Medicine, Stanford, CA, and approved March 3, 2004 (received for review January 7, 2004)

The issue of protein dynamics and its implications in the biological function of proteins are arousing greater and greater interest in different fields of molecular biology. In cryo-electron tomography experiments one may take several snapshots of a given biological macromolecule. In principle, a large enough collection of snapshots of the molecule may then be used to calculate its equilibrium configuration in terms of the experimentally accessible degrees of freedom and, hence, to estimate its potential energy. This information would be crucial in order to analyze the biological functions of biomolecules by directly accessing the relevant dynamical indicators. In this article, we analyze the results of cryo-electron tomography experiments performed on monoclonal murine IgG2a antibodies. We measure the equilibrium distribution of the molecule in terms of the relevant angular coordinates and build a mechanical model of the antibody dynamics. This approach enables us to derive an explicit expression of the IgG potential energy. Furthermore, we discuss the configuration space at equilibrium in relation to results from other techniques, and we set our discussion in the context of the current debate regarding conformation and flexibility of antibodies.

It is now widely recognized that proteins are flexible objects and exist in populations of different structures, rather then in a single rigid conformation. In fact, collective motions of domains greatly enhance proteins' ability to bind other molecules. Textbooks usually show proteins naked, neglect crucial dynamical aspects such as fluctuations, and take little notice of the protein environment. Real proteins, however, are wiggling and jiggling, dressed by the hydration shell, and usually embedded in a cell or cell membrane (1).

Antibodies link antigens and immunological effector systems by means of highly mobile linkers that connect the hypervariable antigen-binding sites to the effector domain (Fc). Antibodies possess the structural flexibility to adapt to a huge variety of antigen shapes and sizes, whereas they share similar conserved Fc regions that interact with a limited number of effector systems, such as Fc receptors and complement (2, 3).

The antibody IgG is a glycoprotein with a molecular mass of 150 kDa, which binds to foreign agents such as viruses by subunits named fragment antigen-binding arms (Fab arms). Hinges connect two Fab arms to a stem that crystallizes easily ("Fc" stem), so that each antibody can bind to two antigens or to a single antigen with increased strength. It is known that the arms of the uncomplexed IgGs are highly flexible and have a wide range of variability of the reported values of Fab–Fab and Fab–Fc angles (4).

Two-dimensional electron microscopy and physiochemical experiments also support a hypothesis of inherent flexibility of the IgG molecules (4, 5). However, a great variability exists in the literature as to the average values of crucial structural parameters such as Fab–Fab and Fab–Fc angles (6); and, to our knowledge, no estimate exists of their probability distribution at equilibrium. Large-scale conformational differences have also been detected among three complete structures of intact and functional antibodies (subclasses human IgG1, murine IgG1, and murine IgG2a) solved by x-ray crystallography (6, 7). These differences are due, in part, to the high fragility of the IgG molecules and, more generally, to the limitations intrinsic to experimental techniques such as electron microscopy and x-ray analysis.

Electron microscopy analysis preceded crystallographic analysis (8, 9) of immunoglobulins by more than a decade and, for a time, has been the only way to analyze their 3D structure (see ref. 4 for a review). Once the x-ray structures were deduced, the role of electron microscopy gradually moved from gross structural analysis to address more sophisticated structural and functional questions. However, electron micrographs are 2D representations and necessarily present projected images, making interpretation in three dimensions very difficult. On the other hand, x-ray crystallography suffers from the inherent ambiguities associated with unpredictability of differential packing environments within the crystals. Electron tomography is a general method for 3D reconstruction of individual objects from a tilt series of electron microscope images (10–13). The electron tomography method is general in the sense that it can be applied to any transparent object (14–16); it is not restricted to symmetrical or regularly arranged objects (17–19) or to objects with a preferred orientation on a support grid (20, 21).

In cryo-electron tomography (cryo-ET) experiments the sample is quenched to the temperature of liquid nitrogen. Therefore, one gets a *gallery* of instantaneous snapshots of the system. In ref. 11, data from cryo-ET of individual IgG molecules in solution have been analyzed and have confirmed that the position of the Fab arms relative to the Fc stem may greatly differ from one molecule to another. In this article, we analyze a subset of high-resolution 3D snapshots from the same set of experiments. Our aim is 2-fold: reconstruct the equilibrium statistics of the principal structural parameters and use such information as the starting point for studying the dynamics of an individual immunoglobulin in solution. Hence, we first analyze the experimental images and introduce a statistical description of the IgG configuration. This study enables us to deduce our first important result, namely, the probability distributions of the Fab–Fab and Fab–Fc angles. We then build a simple mechanical model and derive an effective potential energy for the single antibody, which also allows us to calculate quantitative estimates of the relevant frequencies of the IgG motion. This model is the main result of this article.

In the following sections, we introduce our model and perform an analysis of the experimental data. We then detail the results and we summarize our findings and sketch the developments of the present work. The experimental method and the details of the imaging process are outlined in *Appendix 1*, which is published as supporting information on the PNAS web site.

The Model

The phase space of a system with n degrees of freedom can be parameterized by a vector $(\vec{q}, \vec{p})$ of n generalized coordinates

This paper was submitted directly (Track II) to the PNAS office.

Abbreviations: cryo-ET, cryo-electron tomography; Fab arms, fragment antigen-binding arms.

†L.B., D.F., and F.P. contributed equally to this work.

¶To whom correspondence should be addressed. E-mail: ulf.skoglund@cmb.ki.se.

$(q_1, \ldots, q_n)$ and n conjugate momenta $(p_1, \ldots, p_n)$, containing the information about the system configuration and velocity, respectively. When the system is in equilibrium with a thermal bath at temperature T, any point in the phase space can be occupied with a probability density

$$\rho(\vec{q}, \vec{p}) = \frac{1}{Z(T)} \exp\left[-\frac{K(\vec{q}, \vec{p}) + V(\vec{q})}{k_B T}\right], \qquad [1]$$

where K is the kinetic energy, V is the system potential, k_B is the Boltzmann constant, and $Z(T)$ is a temperature-dependent normalization factor. It is important to notice that, whereas in Cartesian coordinates the kinetic energy only depends on momenta, in general, it also depends on coordinates (as in the case of polar coordinates).

If the equilibrium probability density of a system is made accessible experimentally, it is in principle possible to invert Eq. **1** to extract information regarding the dynamical properties of the system. This possibility is the case in cryo-ET experiments, where a direct measure of the equilibrium distribution in the configuration space can be performed through a statistical analysis of an ensemble of different snapshots of the system. The equilibrium probability distribution in the configuration space results from the integration of Eq. **1** over the conjugate momenta p_i:

$$\rho(\vec{q}) = \frac{1}{Z(T)} \exp\left[-\frac{V(\vec{q})}{k_B T}\right] S(\vec{q}), \qquad [2]$$

where

$$S(\vec{q}) = \int \exp\left[-\frac{K(\vec{q}, \vec{p})}{k_B T}\right] dp_1 \ldots dp_n. \qquad [3]$$

The function $S(\vec{q})$ is the kinetic contribution to the equilibrium probability density and must be computed analytically to extract the potential from the measured $\rho(\vec{q})$. Once this analysis is done, we can calculate the potential V as:

$$V(\vec{q}) = -k_B T \ln\left[\frac{\rho(\vec{q})}{S(\vec{q})}\right] + V_0(T), \qquad [4]$$

where $V_0(T)$ is a constant, which depends only on temperature. We stress that the temperature enters Eq. **4** as a parameter. In particular, it should be noted that the derivation of Eq. **4** is rigorous only if the system is at thermodynamic equilibrium (at the temperature T). In general, the validity of this condition and the appropriate value of T that characterizes the collection of snapshots depend on the timescales set by both the experiment and the system dynamics.

In our model, we consider the immunoglobulin molecule to be composed of three rigid rods freely jointed together in a common point (Fig. 1): namely, two (Fab) arms of equal mass M and length L and the (Fc) stem (pictorially, it may be visualized as a *lobster*). As a first approximation, we assume the three bodies to be connected in a single point and therefore neglect the translational offsets among the intersections of the Fab and Fc major axes. Furthermore, at this level of schematization, we do not take into account the intra-Fab distortions associated with flexion of the elbow regions. The Fc rod is aligned along the z axis and two angles are introduced to specify the position of each Fab relative to the Fc. The angles θ_i $(i = 1, 2)$ are measured on the plane perpendicular to the Fc and identify the position of the Fab–Fc planes. The position of the Fab arms within those planes is then measured by the angles ϕ_i $(i = 1, 2)$. Moreover, we denote with ξ the Fab–Fab separation in the Fab–Fab plane.

In the following text, we choose to parametrize the system as a function of the angles $\vec{\Omega} = (\phi_1, \phi_2, \theta_1, \theta_2)$ and the associated

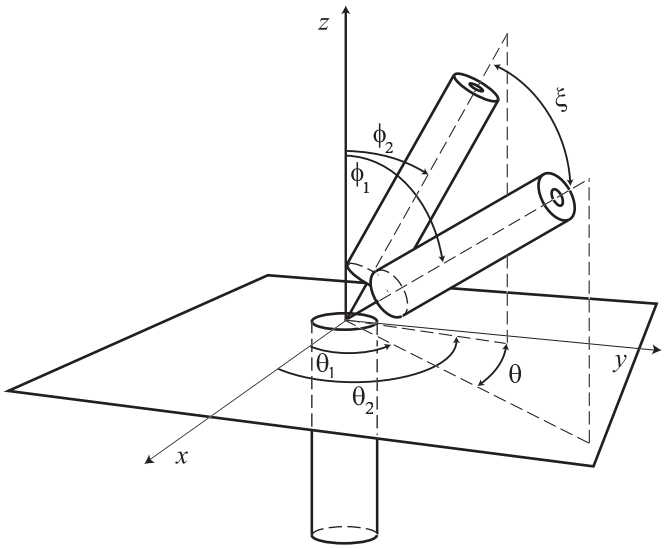

Fig. 1. Coarse-grained model of an immunoglobulin molecule. The two Fab arms and the Fc are replaced by rigid rods freely jointed in the hinge region. The relative position of the $Fab_{1,2}$–Fc arms is described by the two angles ϕ_i and θ_i $(i = 1, 2)$, in the Fab_i–Fc planes and in the plane perpendicular to Fc, respectively. The angle ξ measures the Fab–Fab separation in the Fab–Fab plane.

conjugate momenta (actions) $\vec{\mathcal{J}} = (J_{\phi_1}, J_{\phi_2}, J_{\theta_1}, J_{\theta_2})$. In this case, the mathematical derivation of the Hamiltonian is straightforward and we get:

$$\mathcal{H}(\vec{\Omega}, \vec{\mathcal{J}}) = K(\vec{\Omega}, \vec{\mathcal{J}}) + V(\vec{\Omega}), \qquad [5]$$

where

$$K(\vec{\Omega}, \vec{\mathcal{J}}) = \frac{1}{2I}\left[J_{\phi_1}^2 + J_{\phi_2}^2 + \frac{J_{\theta_1}^2}{\sin^2 \phi_1} + \frac{J_{\theta_2}^2}{\sin^2 \phi_2}\right], \qquad [6]$$

and I is the moment of inertia of a rod about an axis perpendicular to its end.

Let us stress that the choice of the set of variables $\vec{\Omega}$ is not unique. A sensible alternative to our choice might well be to consider the Fab–Fab angle ξ (see Fig. 1), e.g., by adopting the set of coordinates $(\phi_1, \phi_2, \theta_1, \xi)$. However, we note that, for any given values of ϕ_1 and ϕ_2, the angle ξ is confined to the interval $|\phi_1 - \phi_2| < \xi < \phi_1 + \phi_2$. As a consequence, one must take such *entropic* constraint into account in the derivation of Eq. **2** making the analytical calculation much more cumbersome.

The function $S(\vec{\Omega})$ can be computed by inserting the expression 6 into Eq. **3**. After the integration we obtain:

$$V(\vec{\Omega}) = -k_B T \ln\left[\frac{\rho(\vec{\Omega})}{\sin \phi_1 \sin \phi_2}\right], \qquad [7]$$

where we have dropped the temperature-dependent additive constant.

In the next section we first illustrate the derivation of the equilibrium density $\rho(\vec{\Omega})$ from the experimental data and then discuss its statistical analysis.

Analysis of the Experimental Data

By using cryo-ET, we were able to reconstruct 3D volumes of IgG molecules in solution. The analysis of the reconstructed volumes allowed us to isolate 42 reliable structures of individual molecules. We operated the selection according to strict criteria: the objects that did not present a fully resolved structure were rejected. In particular, for all selected molecules, the Fc was

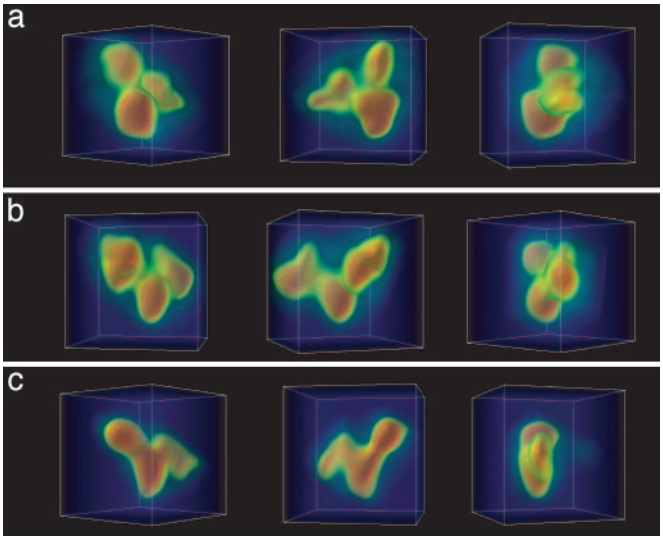

Fig. 2. Gallery of individual IgG molecules visualized by volume rendering in three dimensions. Three different views of each tomogram are displayed. The box is 50 × 40 × 50 pixels.

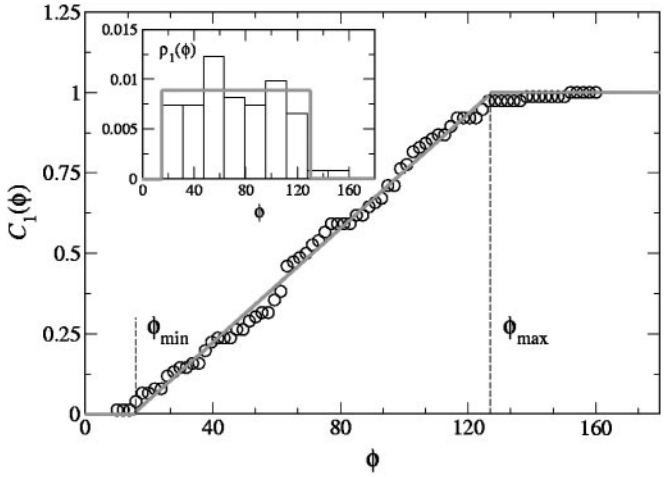

Fig. 3. Experimental cumulative distribution of the ϕ_1, ϕ_2 angles (○) and fit with the function $C_1(\phi) = \int_0^{\phi} \rho_1(\phi')\, d\phi'$ (red solid line). (*Inset*) Normalized histogram of the experimental data and plot of the square function 9 with $\phi_{min} \approx 15°$ and $\phi_{max} \approx 127.6°$ (red solid line).

identified and the broadening of the upper part of the segment clearly displayed. However, it was not possible to align consistently the Fc stems, and thus we could not systematically label the "left" and "right" Fab domains.

A typical gallery of reconstructed, individual IgG molecules is shown in Fig. 2. The densities are mapped with a continuous color coding, ranging from blue to red, clearly highlighting the large-scale structure of the antibody.

For each molecule, we measured the Fab–Fab angle ξ and the two Fab–Fc angles ϕ_1 and ϕ_2 by approximating the three domains with ellipsoidal envelopes and measuring the angles formed by their major axes.

As already discussed in *The Model*, we parametrize the system in the space $(\phi_1, \phi_2, \theta_1, \theta_2)$. However, we are interested in the relative motion of the two Fab arms. As a consequence, we consider the transformation to the relative coordinates $\theta = \theta_2 - \theta_1$ and $\psi = [\theta_2 + \theta_1]/2$, while keeping ϕ_1 and ϕ_2. The angle ψ describes the motion of the center of mass of the two Fab arms projected on a plane perpendicular to the Fc stem. However, we recall that the "front" and "back" sides of the Fc domain are not distinguishable within our experimental resolution. Consequently, it appears reasonable to consider the probability $\rho(\phi_1, \phi_2, \theta) = \langle \rho(\phi_1, \phi_2, \theta, \psi) \rangle_{\psi}$, averaged over ψ in the domain [0, 360°]. We note that, by doing this, we are also neglecting whatever energy is associated with a torsion of the two Fab arms as a whole with respect to the Fc axis.

We now wish to estimate the density profile $\rho(\phi_1, \phi_2, \theta)$ from the experimental data. The available population of our configurational ensemble is limited. Therefore, we have enough statistics to only access the coordinate space ϕ_1, ϕ_2, θ one angle at a time. Furthermore, we are not able to distinguish between the two Fab domains. Consequently, each molecule contributes two values to the population of the Fab–Fc angles. Accordingly, we assume that the density $\rho(\phi_1, \phi_2, \theta)$ can be factorized as the product of three 1D normalized functions in the following fashion[‖]:

$$\rho(\phi_1, \phi_2, \theta) = \rho_1(\phi_1)\rho_1(\phi_2)\rho_2(\theta). \qquad [8]$$

[‖]An argument to test *a posteriori* the validity of our theoretical framework (including the hypothesis of factorization) is provided in *Appendix 2*, which is published as supporting information on the PNAS web site.

We show in Fig. 3 the normalized histogram of the experimental data $\rho_1(\phi)$ with $\phi_1 = \phi_2 = \phi$ (*Inset*) and the corresponding normalized cumulative distribution. The latter is easily calculated from the data by noting that it is nothing but the rank-frequency plot with the axes inverted. In general, it is preferable to work with the cumulative distributions, because the low-statistics regions get more populated with the integration. The experimental data can be clearly interpreted by means of the uniform distribution in the interval $[\phi_{min}, \phi_{max}]$:

$$\rho_1(\phi) = \begin{cases} \dfrac{1}{\phi_{max} - \phi_{min}} & \phi_{min} < \phi < \phi_{max} \\ 0 & \text{otherwise.} \end{cases} \qquad [9]$$

To determine the experimental cutoffs ϕ_{min} and ϕ_{max}, we fitted the experimental cumulative distribution. From the fit we found $\phi_{min} \approx 15°$ and $\phi_{max} \approx 127.6°$.

The projected angles θ can be straightforwardly obtained from the experimental values of ϕ_1, ϕ_2, and ξ. They are measured in the interval [0, 180°], because we cannot systematically identify the front and back broad sides of the Fc domain in the reconstructed data. Therefore, to extend the distribution domain to the interval [180°, 360°], we perform a reflection of the data around $\theta = 180°$. In Fig. 4 we show the normalized histogram $\rho_2(\theta)$ (*Inset*) and the corresponding normalized cumulative distribution. We found that a simple Lorentzian profile truncated in [0,360°] fitted the data extremely well:

$$\rho_2(\theta) = \frac{1}{2\sigma_\theta \operatorname{atan}(\theta_0/\sigma_\theta)} \left[1 + \left(\frac{\theta - \theta_0}{\sigma_\theta} \right)^2 \right]^{-1}, \qquad [10]$$

where $\theta_0 = 180°$, and σ_θ is the only floating parameter. As we did for the $\rho_1(\phi)$, we determined σ_θ by fitting the experimental cumulative distribution. From the fit we found $\sigma_\theta \approx 91.6°$.

The Effective Potential

We are now able to compute the effective potential $V(\phi_1, \phi_2, \theta)$. By using Eqs. **8**, **9**, and **10**, Eq. **7** can be written in the following manner:

$$V(\phi_1, \phi_2, \theta) = V_1(\phi_1) + V_1(\phi_2) + V_2(\theta), \qquad [11]$$

where

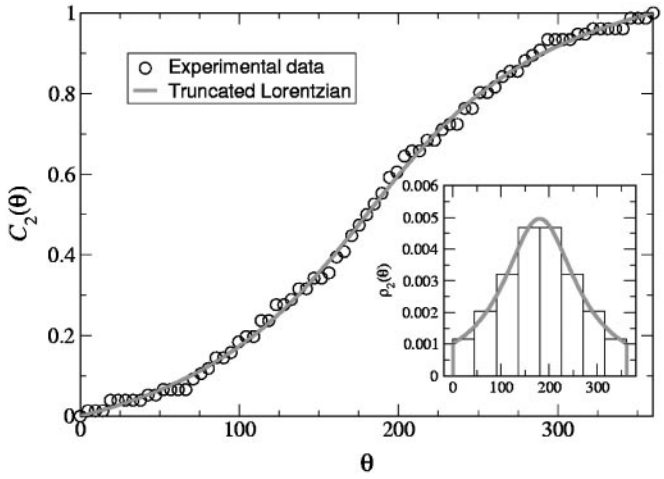

Fig. 4. Experimental cumulative distribution of the θ angles (○) and fit with the function $C_2(\theta) = \int_0^\theta \rho_2(\theta')\, d\theta'$ (red solid line). (*Inset*) Normalized histogram of the experimental data and plot of the truncated Lorentzian 10 with $\sigma_\theta \approx 91.6°$.

$$V_1(\phi) = k_B T_0[\ln(\sin\phi)]$$
$$V_2(\theta) = k_B T_0 \ln\left[1 + \left(\frac{\theta - \theta_0}{\sigma_\theta}\right)^2\right]. \qquad [12]$$

As already mentioned, the temperature T_0 is here a constant parameter. More precisely, the angular distributions obtained from the experimental snapshots of the IgG molecules are to be considered estimates of the equilibrium configuration at a temperature T_0. (For a detailed description, see *Appendix 3*, which is published as supporting information on the PNAS web site.)

The potential $V_1(\phi)$ describes the motion of the two Fab arms in the Fab–Fc planes. It arises from the combination of the flat experimental distribution of the ϕ angles and the centrifugal term from the integration of the kinetic part of the Hamiltonian (Fig. 5).

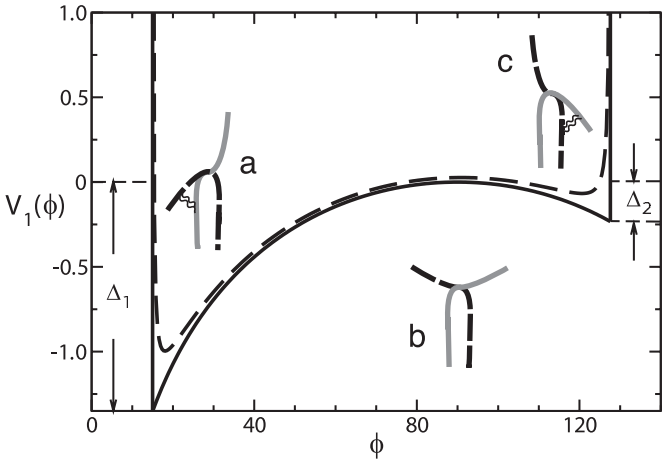

Fig. 5. Solid line shows potential energy in the Fab–Fc planes (units of $k_B T_0$). The experimental values of the angular cutoff $\phi_{min} \approx 15°$ and $\phi_{max} \approx 127.6°$ are explicitly drawn as rigid walls. Dashed line shows smoothed potential (see text). The relative Fab–Fc position is also represented in the two wells and at the barrier as a sketch of the two heavy chains mutually crossing in the hinge region.

We are now able to understand the experimental evidence of equiprobability of any ϕ values in the Fab–Fc planes. It is the combined effect of two different competing energy terms. On the one side, the centrifugal term favors configurations at values close to $\phi = 90°$. In fact, the rotation around the Fc axis of a Fab arm in such configurations has the lowest kinetic energy. On the other side, one has the potential energy $V_1(\phi)$. It may be speculated that the latter in turn arises from the combination of two distinct energy terms. A greater and greater price is paid the more the chains are bent in the hinge region. However, an energy gain may also occur in some configurations in terms of contacts between the CH1 and CH2 subdomains. As a result, we can sketch the trend of $V_1(\phi)$ as the a single arm moves from ϕ_{min} to ϕ_{max} in the following fashion. Let us represent the IgG molecule at the simple level of two mutually crossing identical (heavy) chains and isolate one of them for reference (Fig. 5, red chain). The configuration at ϕ_{min} has the lowest energy, which means that, even though no new contacts can be formed in this configuration, there is also no bending energy price to pay at all (configuration a). The more the Fab rotates toward the Fc, the more it costs to be bent. In particular, it takes about $2k_B T_0$ to bend the chain at an angle $\phi = 90°$ (configuration b). However, some energy may be regained past $\phi = 90°$ in terms of the new contacts made available, which gives a gain of about $k_B T_0/2$ (configuration c). This makes $\phi \approx 90°$ a barrier that separates two local minima at $\phi \approx \phi_{min}$ and $\phi \approx \phi_{max}$.

The combined effect of this double-minimum energy landscape and the centrifugal energy result in a uniform distribution of the Fab–Fc angles. As we show in *Appendix 2*, the two Fab arms are characterized by an average separation $\xi \approx 110°$. Translated into the ϕ domain, this information means that the two local minima at $\phi \approx \phi_{min}$ and $\phi \approx \phi_{max}$ are occupied by one Fab at a time.

Of course, the *true* potential will be a smooth function of ϕ in the two binding regions. An example of what a more realistic $V_1(\phi)$ might look like is the dashed curve in Fig. 5, which is the graph of the function

$$V_1(\phi) = 2k_B T_0\left\{\ln(\sin\phi) + \frac{1}{(\phi - \phi_{min})} + \frac{1}{(\phi_{max} - \phi)}\right\}, \qquad [13]$$

where the rigid walls have been replaced by moderate (ϕ^{-1})-like repulsive terms. The smoothing of the rigid walls causes the two cuspids at $\phi = \phi_{min}$ and $\phi = \phi_{max}$ to become new differentiable minima at $\phi \approx 20°$ and $\phi \approx 117°$.

By using Eq. **13**, we can estimate the characteristic frequencies ω_ϕ associated with small oscillations in the two wells as $\omega_\phi \approx \sqrt{\kappa_\phi/I} = \sqrt{3\kappa_\phi/ML^2}$, where $\kappa_\phi = V_1''(\phi)$ evaluated at the bottom of the well, while $M \approx 8 \times 10^{-23}$ kg and $L \approx 80$ Å are the Fab mass and length, respectively. We get $\omega_{\phi_{min}} \approx 7.1 \times 10^8 \sqrt{T_0}\ s^{-1}$ and $\omega_{\phi_{max}} \approx 1.9 \times 10^8 \sqrt{T_0}\ s^{-1}$.

For small values of $\theta - \theta_0$, the potential energy $V_2(\theta)$ can be expanded as follows:

$$V_2(\theta) \approx \frac{1}{2}\kappa_\theta(\theta - \theta_0)^2, \qquad [14]$$

where we have introduced the elastic force constant

$$\kappa_\theta = \frac{2k_B T_0}{\sigma_\theta^2}. \qquad [15]$$

Therefore, for small displacements about the equilibrium position $\theta_0 = 180°$, $V_2(\theta)$ is an elastic energy that accounts for small oscillations in the plane orthogonal to the Fc. Hence, it describes the deviations from the equilibrium planar Y-like shape of the

BIOPHYSICS

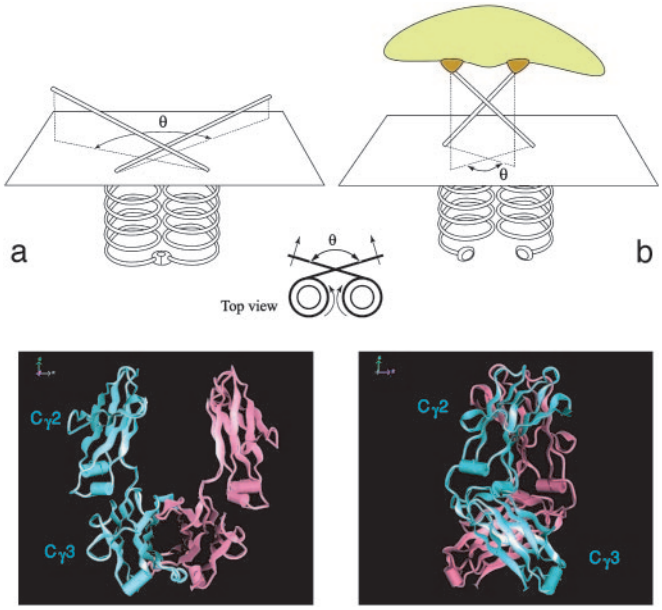

Fig. 6. (*Upper*) Schematization of the halves of an Fc stem. The chains are explicitly shown to cross at the hinge level. (*a*) Unbound antibody. (*b*) Antibody–antigen complex (*Lower*) Two views of the crystal structure of the Fc domain from human immunoglobulin IgG. The two heavy chains have different colors (from the web site of M. Clark, available at www.path.cam.ac.uk/~mrc7/igs/mikeimages.html#Model).

immunoglobulin. We may interpret such elastic energy as sketched in Fig. 6.

With no antigen bound at the Fab-binding sites, antiintegral oscillations of the two Fab arms correspond to rotations of the two halves of the Fc stem against each other around the vertical axis (Fig. 6*a*). Such rotation is in turn opposed by the contacts between the two CH3 immunoglobulin domains at the Fc end (see the crystal structure of the Fc in Fig. 6). The net result is a force that opposes oscillations away from the planar $\theta = 180°$ configuration. On the other hand, we may imagine that, when the antibody binds an antigen, the same elastic energy might be used to weaken the contacts in the Fc tail, thus making it easier for the back region to open up and bind to other molecules. This would be extremely useful, e.g., in the binding process of the antibody–antigen complex to the specific receptors on immune cells (Fig. 6*b*).

We stress that the strength of such elastic force is rather small. This corresponds to a very broad distribution in the range $0 < \theta < 2\theta_0$, with a large standard deviation $\sigma_\theta \approx \theta_0/2$. Correspondingly, we note that the hinges cannot be expected to transmit mechanical energy between the Fabs and Fc domains as perfectly rigid joints because of their intrinsic *bendability*. In other words, only a limited portion of the energy involved in any displacements of either domain will be effectively transferred in the above-mentioned fashion. We may imagine the remaining energy to be evenly *dissipated* in the deformation of the hinges themselves.

The characteristic frequency ω_θ associated with small oscillations in the potential well $V_2(\theta)$ depends, in general, on the values of ϕ_1 and ϕ_2. Yet, we can estimate ω_θ by linearizing the equations of motion of the system in the vicinity of the equilibrium positions of the system. These positions are the two degenerate configurations $\Omega_1 = (\phi_{\min}, \phi_{\max}, \theta_0)$ and $(\phi_{\max}, \phi_{\min}, \theta_0)$, plus the arms-down and arms-up configurations at $\Omega_2 = (\phi_{\max}, \phi_{\max}, \theta_0)$ and $\Omega_3 = (\phi_{\min}, \phi_{\min}, \theta_0)$, respectively. However, we observe that the latter arrangement is assigned a very small probability of occurrence in terms of the corresponding ξ and θ. Hence, we are left with the two characteristic frequencies:

$$\omega_\theta^{[1]} \approx \sqrt{\frac{\kappa_\theta}{2I}} \sqrt{\frac{1}{\sin^2 \phi_{\min}} + \frac{1}{\sin^2 \phi_{\max}}}$$
$$\omega_\theta^{[2]} \approx \sqrt{\frac{\kappa_\theta}{I}} \frac{1}{\sin \phi_{\max}}. \qquad [16]$$

By inserting the best-fit result $\sigma_\theta \approx 91.6°$ in Eq. **15** we get $\omega_\theta^{[1]} \approx 2.3 \times 10^8 \sqrt{T_0}\ \mathrm{s}^{-1}$ and $\omega_\theta^{[2]} \approx 1.1 \times 10^8 \sqrt{T_0}\ \mathrm{s}^{-1}$. However, we observe that the frequency $\omega_\theta^{[1]}$ is nearly twice $\omega_\theta^{[2]}$. As a consequence, it is the latter that should be regarded as the value setting the frequency scale in θ. Unfortunately, the precise value of T_0, in general, will depend in a complicated fashion on the solvent viscosity and the characteristic timescales of the molecular vibrations as compared with the timescale of the temperature quench. To be more precise, the ambient temperature $T_{\mathrm{amb}} \approx 20°\mathrm{C}$ is only an upper bound. On the other hand, a lower bound can be identified at the temperature T_∞, which marks the divergence of water viscosity. At such temperatures, a transition occurs in the solvent from a liquid to a solid (glasslike) phase during the quenching process. We can estimate T_∞ by fitting the experimental values of the water viscosity measured in the interval [0,100°C] (22). We found $T_\infty \approx -45°\mathrm{C}$ (data not shown). Such a value is in excellent agreement with the accepted estimate of the singularity point of liquid water $T_s \approx 228\ \mathrm{K}$, where the C_p, isothermal expansivity and isothermal compressibility all diverge. At that point, it is believed that water becomes a rigid gel with a structure closely resembling that of ice *I*, when quenched at 10^6–10^7°C/s (ref. 23 and references therein and ref. 24).

We remark that the use of the two limiting values T_{amb} and T_∞ in 16 results in a difference of <10% in the estimates of the frequencies of small oscillations. By choosing $T_0 = T_\infty$ we therefore obtain:

$$\omega_\theta \approx 1.6 \times 10^9\ \mathrm{s}^{-1}$$
$$\omega_{\phi_{\min}} \approx 1.0 \times 10^{10}\ \mathrm{s}^{-1} \qquad [17]$$
$$\omega_{\phi_{\max}} \approx 2.9 \times 10^9\ \mathrm{s}^{-1}.$$

Conclusions

In the first part of this work we measured the experimental probability distributions of the relevant angular coordinates of an IgG molecule at equilibrium. We showed that the average value of the Fab–Fab angle is ≈110°. Its distribution is a broad bell-shaped function, with a standard deviation of ≈30°. This finding correlates well with the estimates obtained by other dynamical measurements, such as dielectric relaxation experiments on bovine IgG (25) ($\xi \approx 126°$) and immunoelectron microscopy studies (4) ($\xi = 127 \pm 32°$ for IgG2). A worst agreement is found with the only IgG2 intact structure from x-ray crystallography, namely, murine IgG2A mAb 231 [PDB ID code 1IGT (26)]. We observe that the measured values of the Fab–Fab angle of 172° might be affected by unpredictable errors originating by the special packing environment within the crystal. Of course, this shortcoming of x-ray crystallography is unavoidable when applied to highly flexible systems such as antibodies. The results from the other two x-ray structures of intact IgG antibodies are $\xi \approx 148°$ [PDB ID code 1IGY (27)] and $\xi \approx 117°$ [PDB ID code 1HZH (28)]. However, both the latter molecules are IgG1 antibodies. Consequently, the differences in hinge conformation between IgG1 and IgG2 species do not allow a straight comparison of our results with those structures.

We note that our findings may also point the correct way to normal mode analysis of antibodies, whereby crystal structures modified according to more accurate structural measurements

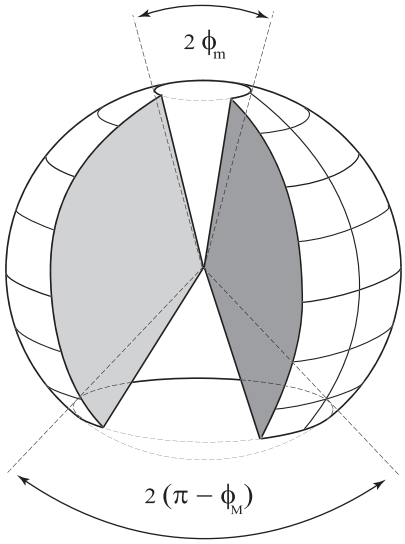

Fig. 7. Representation of the IgG configuration space. The vertical axis of the sphere coincides with the Fc stem; the hinge region lies at its center.

would seem the appropriate equilibrium positions to use in the analysis.

Furthermore, we showed that the Fab–Fc angles are approximately uniformly distributed between the two limiting values $\phi_{min} \approx 15°$ and $\phi_{max} \approx 127.6°$. Such boundaries reflect the excluded-volume steric constraints imposed by the molecular structure. We can give a pictorial description of the configuration space of an IgG molecule by following the spatial arrangement of Fig. 1. The only constraint is $\phi_{min} < \phi_1$ and $\phi_2 < \phi_{max}$. Hence, it is enough to cut away from a sphere of radius L two cones of aperture $2\phi_{min}$ and $2(180° - \phi_{max})$, respectively (Fig. 7). Therefore, no matter where the Fab arms are positioned with respect to the Fc, the molecule always has two accessible regions. The extension of the banned regions can be quantified in terms of the corresponding solid-angle fractions as

$$f_m = \frac{1}{4\pi}\int_0^{2\pi} d\theta \int_0^{\phi_m} d\phi \approx 0.02$$

$$f_M = 1 - \frac{1}{4\pi}\int_0^{2\pi} d\theta \int_0^{\phi_M} d\phi \approx 0.2. \qquad [18]$$

These estimates show that, on average, the IgG molecules prefer to confine the motion of the Fab arms in a region corresponding to ≈80% of the whole solid angle. Of course, an identical scenario holds at any position of the Fc stem with respect to a given absolute reference frame. In summary, the angular distance between either Fab and the Fc cannot be smaller than ≈50°. This fact may have interesting implications in the neutralization mechanisms of the antigen–antibody complexes, which require the interaction of the Fc domain with different biological units, such as specific receptors on immune cells.

In the second part of the work, we established a connection between the measured angular distributions and the dynamics of the antibody. In particular, we derived an explicit expression for the potential energy function of the molecule based on a simple mechanical model. The inverse path may then be taken to investigate the equilibrium distribution of a single IgG in solution through computer simulation of its Langevin dynamics. Preliminary results (not reported here) confirm the consistency of our procedure. In particular, the dynamical approach opens the way to direct access to different dynamical indicators, potentially linked to the biological functions of the antibody. These indicators include two-point time-correlation functions between selected degrees of freedom, such as Fab–Fab angles and Fab–Fc angles or Fab1–Fc and Fab2–Fc angles. In addition, straight access to the molecule dynamics may be used for comparison with results from different experimental techniques, such as dielectric relaxation measurements or fluorescence resonance energy transfer microscopy.

L.B. received financial support from Ente Cassa di Risparmio di Firenze.

1. Fenimore, P. W., Frauenfelder, H., McMahon, B. H. & Parak, F. G. (2002) *Proc. Natl. Acad. Sci. USA* **99,** 16047–16051.
2. Burton, D. R. (1985) *Mol. Immunol.* **22,** 161–206.
3. Burton, D. R. (1990) *Trends Biochem. Sci.* **15,** 64–69.
4. Roux, K. (1999) *Int. Arch. Allergy Immunol.* **120,** 85–99.
5. Nezlin, R. (1990) *Adv. Immunol.* **48,** 1–40.
6. Saphire, E. O., Stanfield, R. L., Max Crispin, M. D., Parren, P. W. H. I., Rudd, P. M., Dwek, R. A., Burton, D. R. & Wilson, I. A. (2002) *J. Mol. Biol.* **319,** 9–18.
7. Harris, L. J., Larson, S. B., Skaletsky, E. & McPherson, A. (1998) *Immunol. Rev.* **163,** 35–43.
8. Huber, R., Deisenhofer, J., Colman, P. M. & Matsushima, M. (1976) *Nature* **264,** 415–420.
9. Silverton, E. W., Navia, M. A. & Davies, D. R. (1977) *Proc. Natl. Acad. Sci. USA* **74,** 5140–5144.
10. Skoglund, U., Andersson, K., Strandberg, B. & Daneholt, B. (1986) *Nature* **319,** 560–564.
11. Sandin, S., Öfverstedt, L.-G., Wikström, A.-C., Wrange, Ö. & Skoglund, U. (2004) *Structure (London)* **12,** 409–415.
12. Gilbert, P. F. C. (1972) *Proc. R. Soc. London Ser. B* **182,** 89–102.
13. Hoppe, W., Gassmann, J., Hunsmann, N., Schramm, H. J. & Sturm, M. (1974) *Hoppe-Seyler's Z. Physiol. Chem.* **355,** 1483–1487.
14. Skoglund, U. & Daneholt, B. (1986) *Trends Biochem. Sci.* **11,** 499–503.
15. Frank, J. (1995) *Curr. Opin. Struct. Biol.* **5,** 194–201.
16. Skoglund, U., Öfverstedt, L.-G. & Daneholt, B. (1997) in *RNP Particles, Splicing and Autoimmune-Diseases,* ed. Schenkel, J. (Springer, Heidelberg), pp. 72–94.
17. De Rosier, D. J. & Klug, A. (1968) *Nature* **217,** 130–134.
18. Crowther, R. A., De Rosier, D. J. & Klug, A. (1970) *Proc. R. Soc. London Ser. A* **317,** 319–340.
19. De Rosier, D. J. & Moore, P. B. (1970) *J. Mol. Biol.* **52,** 355–369.
20. Radermacher, M., Wagenknecht, T., Verschoor, A. & Frank, J. (1987) *J. Microsc. (Oxford)* **146,** 113–136.
21. Radermacher, M. (1988) *J. Electron Microsc. Technol.* **9,** 359–394.
22. Lide, D. R., ed. (1995) *CRC Handbook of Chemistry and Physics* (CRC Press, Boca Raton, FL), p. F-40.
23. Kanno, H., Yokoyama, H. & Yoshimura, Y. (2001) *J. Phys. Chem. B.* **105,** 2019–2026.
24. Speedy, R. J. (1982) *J. Phys. Chem. B* **86,** 982–991.
25. Hayashi, Y., Miura, N., Isobe, J., Shinyashiki, N. & Yagihara, S. (2000) *Biophys. J.* **79,** 1023–1029.
26. Harris, L. J., Larson, S. B., Hasel, K. W. & McPherson, A. (1997) *Biochemistry* **36,** 1581–1597.
27. Saphire, E. O., Parren, P. W. H. I., Pantophlet, R., Zwick, M. B., Morris, G. M., Rudd, P. M., Dwek, R. A., Stanfield, R. L., Burton, D. R. & Wilson, I. A. (2001) *Science* **293,** 1155–1159.
28. Harris, L. J., Skaletski, E. & McPherson, A. (1995) *Proteins Struct. Funct.* **23,** 285–289.

The Experimental Method

In our experiments, monoclonal murine IgG2a (1mg/ml) (1, 2), in 10 mM Tris HCl buffer solution at pH 8.0, were mixed 2 : 1 with 10 nm colloidal gold particles. A 4 μl droplet of the suspension were deposited on a grid, blotted with filter paper and plunged into liquid ethane to produce a 50-70 nm vitrified film (3). In practice, the solvent water around the sample is frozen in place, and the sample is cryogenically protected. The usage of a liquid ethane (the melting point is $-188°$C) as a freezing agent prevent the frozen water from forming crystals of cubic ice. The plunging was performed in a climate chamber with humidity of about 80%. The grid was then moved into a Field Emission Gun (FEG) 200 KeV transmission electron microscope (Philips CM200) and kept cool at about the liquid nitrogen temperature (about $-195°$C).

A series of transmission Electron Microscope images was then produced, by tilting the specimen $\pm 60°$ degrees and acquiring the data at either every, or every second degree (2). The micrographs were recorded on a CCD detector at a magnification of 26715 times, thus resulting in a final pixel size of 5.24 Å. In order to minimize the radiation damage, the final total electron dose was kept below the threshold value of ~ 20 e/Å^2 and a post-image check was systematically performed to exclude visible damage during the data collection process.

The $2D$ pictures were then combined together to obtain the full $3D$ volume, using the principle of filtered back projection. To avoid numerical artifacts, which could dramatically affect the final reconstruction, the images need to be properly aligned. For this purpose, the 10 nm colloidal gold particles were used as a reference: their positions were measured for each tilted projection, and this information used to deduce the relative orientation of the planes. The $3D$ density was then further refined by applying the Constrained Maximum Entropy Tomography (COMET) image processing (4). The COMET implementation has been previously tested on the structurally well defined Adeno virus (4) and hnRNP in the Balbiani ring genes from dipteran of Chironomus Tentans (5) and it was shown to reduce the degenerative effect of noise, thus allowing more details to be included in the tomograms.

To validate the analysis we also created pseudo atomic models by making use of quantitative multi-resolution docking algorithms (6). High resolution maps from the crystal structure were docked into the tomograms, and display remarkably good agreement (see Fig. 1).

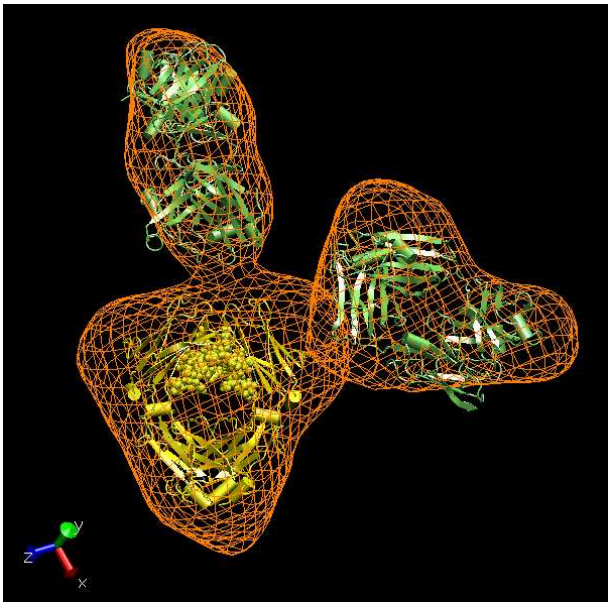

Figure 1: Pseudo atomic model of IgG. The (modified) crystal structure (green Fab; yellow Fc) is shown docked into the tomograms (orange wire frames) (2).

References

1. Okret, S., Wikstrom, A. C., Wrange, O., Anderson, B. & Gustafsson, J. A. (1984) *Proc. Natl. Acad. Sci. USA* **81**, 1609-1613.

2. Sandin, S., Öfverstedt, L.-G., Wikström, A.-C., Wrange, Ö & Skoglund, U. (2004) *Structure*, **12**, 409-415.

3. Adrian, M., Dubochet, J., Lepault, J. & McDowall, A. W. (1984) *Nature* **308**, 32-36.

4. Skoglund, U., Öfverstedt. L.-G., Burnett, R. M. & Bricogne, G. (1996) *J. Struct. Biol.* **117**, 173-188.

5. Wetterberg, I., Zhao, J., Masich, S., Wieslander, L. & Skoglund, U. (2001) *EMBO J.* **20**, 2564-2574.

6. Chacon, P. & Wriggers, W. (2002) *J. Mol. Biol.* **317**, 375-384.

The Probability Distribution of the Fab–Fab Angles: A Coherence Test of the Model

In this appendix we study the distribution of the Fab–Fab angles, which we label with $\rho_3(\xi)$. The experimental profile is shown in Fig. 1 *a* inset: It displays a clear bell–shaped trend with a peak in the region $[100\,^\circ, 120\,^\circ]$. Correspondingly, the cumulative distribution follows a characteristic sigmoid trend.

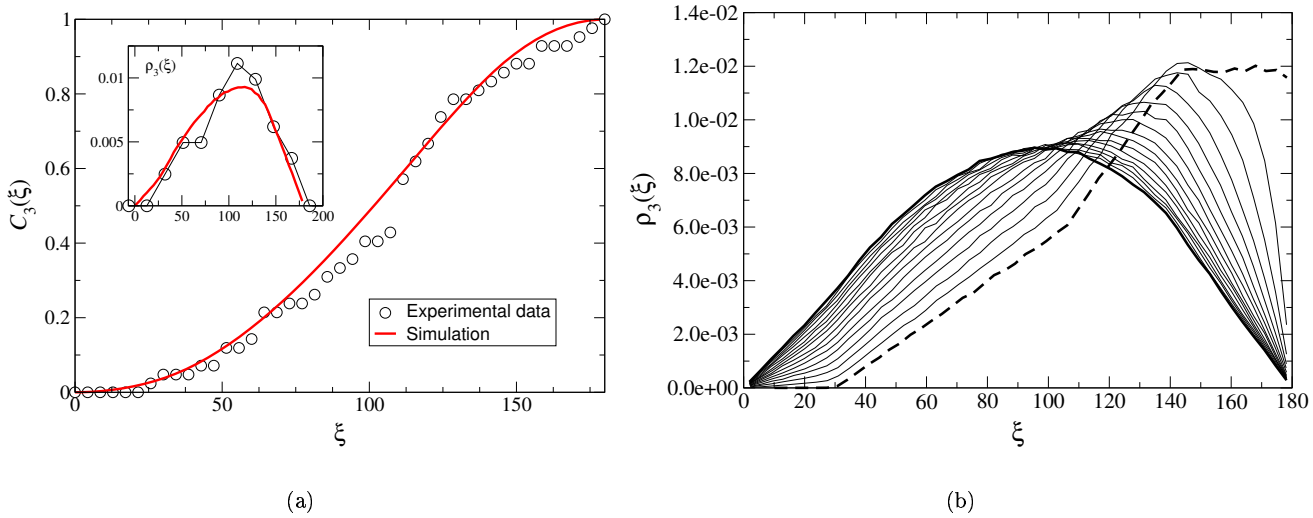

(a) (b)

Figure 1: *(a)* Experimental cumulative distribution of the ξ angles (circles) and normalized histogram (inset, circles). The red lines are the result of a simulation performed according to the distributions $\rho_1(\phi)$ and $\rho_2(\theta)$ calculated from the experimental data. *(b)* Normalized histograms of the ξ angles from simulations performed at different values of σ_θ, from $\sigma_\theta = 0.001$ (thick dashed line) to $\sigma_\theta = 150$ (thick solid line).

Let us consider the hypotheses that underlie the interpretation of our experimental data. It is useful to schematically re-list our assumptions in logical order: *(i)* legitimation to introduce a *reduced* distribution function by averaging on the coordinate $\psi = (\theta_1 + \theta_2)/2$, *(ii)* factorization in the space (ϕ_1, ϕ_2, θ), *(iii)* symmetry of the function $\rho_2(\theta)$ around $\theta = 180\,^\circ$, *(iv)* doubling of the Fab–Fc angles population, $\phi_1 = \phi_2 = \phi$. By construction, the distribution $\rho_3(\xi)$ is not directly used to deduce the effective potential. Therefore, it is in principle possible to recover the information contained in the statistics of the Fab–Fab angles in order to assess *a posteriori* the correctness of the hypotheses built in our model. We proceeded as follows.

We first generated a large number of triplets (ϕ_1, ϕ_2, θ) drawn from the best–fit distributions $\rho_1(\phi)$ and $\rho_2(\theta)$, each triplet corresponding to a certain (possible) orientation of the two Fab arms with respect to the Fc stem. At each point we calculated the corresponding value of ξ. Lastly, we calculated the corresponding histogram and cumulative distribution of the ξ values. The result of this test is plotted in Fig. 1 *a*, showing a very good agreement of the simulation with the experimental distribution. We conclude that there are no potential energy terms responsible for the observed distribution of the Fab–Fab angles. Rather, the latter may be regarded as originating from two different kinds of constraints imposed by the molecular structure. On one side, the excluded volume effects of the Fab–Fab and Fab–Fc interactions result in the appearance of the experimental cutoffs $\phi_{\min} \approx 15\,^\circ$ and $\phi_{\max} \approx 127.6\,^\circ$. On the other side, the distribution $\rho_2(\theta)$ must have a standard deviation in the neighborhood of the experimental σ_θ to produce the observed $\rho_3(\xi)$ in combination with the distribution $\rho_1(\phi)$, namely $\sigma_\theta \approx 90\,^\circ$. This fact is illustrated by the curves shown in Fig. 1 *b*, which are produced in obeyance to the same geometrical constraints, but at different values of σ_θ.

In conclusions, we can interpret the results of the above described test as a proof of coherence of our theoretical framework.

The Equilibrium Distribution at Room Temperature

As we stated in Analysis of the Experimental Data, the validity of our approach strongly depends on the assumption that the gallery of snapshots describes a system at thermodynamical equilibrium. This assumption should be carefully checked in the case of a system that undergoes a temperature quench between room temperature ($T_{\rm amb} \simeq 20^{\rm o}$C) and the temperature of dynamical arrest (estimated as the temperature of divergence of water viscosity $T_\infty \simeq -45^{\rm o}$C).

We can identify two limiting cases for this process. In the case of an almost instantaneous temperature quench the probability density of states of the system would not have the time to significantly relax away from the equilibrium distribution at room temperature. The latter one would then be the distribution of states observed in the experiment. In the opposite case of an almost adiabatic temperature quench, the system would have time to gradually thermalize and it will approach the equilibrium distribution at T_∞ through a series of consecutive quasi-equilibrium states. At realistic values of the quenching rate, the situation will be a compromise between these two extremes, so that the observed density of states would correspond as a first approximation to thermodynamic equilibrium at a temperature intermediate between $T_{\rm amb}$ and T_∞.

To gain a quantitative insight into this problem, let us focus on the equilibrium distribution at room temperature in the two limiting cases $T_0 = T_{\rm amb}$ and $T_0 = T_\infty$. By introducing in Eq. **2** the Eqs. **11** and **12** for the effective potential, one obtains the following relation:

$$\rho(\phi_1, \phi_2, \theta, T_{\rm amb}) = \frac{1}{Z(T_{\rm amb})} \left[\sin\phi_1 \sin\phi_2\right]^{1-T_0/T_{\rm amb}} \left[1 + \left(\frac{\theta-\theta_0}{\sigma_\theta}\right)^2\right]^{-T_0/T_{\rm amb}} \qquad (1)$$

where $\phi_{\rm min} < \phi_1, \phi_2 < \phi_{\rm max}$ and $\theta \in [0, 360]$. The normalized profiles $\rho_1(\phi, T_{\rm amb})$ and $\rho_2(\theta, T_{\rm amb})$, and their corresponding cumulative distributions, are computed from Eq. **1** and plotted in Figures 1 *a* and *b*, respectively. The two distributions differ only slightly. More precisely, the difference between them is smaller than the average fluctuation displayed by the experimental data (i.e. statistical error). As a consequence, we can claim that the measured distribution is consistent with the stationarity hypothesis.

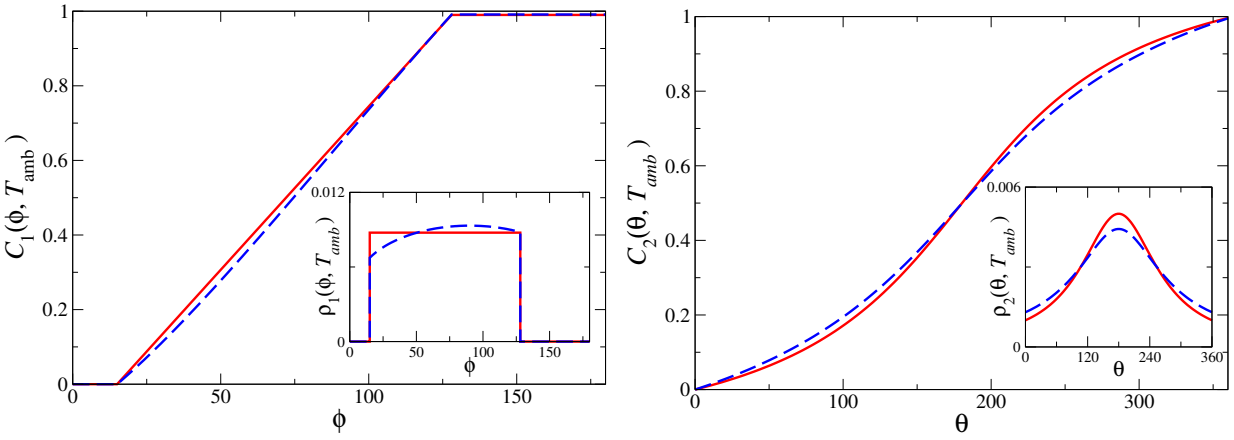

Figure 1: *(a)* Cumulative distributions of the ϕ angles at room temperature (main plot) and associated normalized histograms (inset). Both profiles are computed from Eq. **1**. The solid line refers to $T_0 = T_{\rm amb}$ whereas the dashed line is found by setting $T_0 = T_\infty$. *(b)* Cumulative distributions of the θ angles at room temperature (main plot) and associated normalized histograms (*Inset*). The curves are derived from Eq. **1**. The solid line refers to $T_0 = T_{\rm amb}$ while the dashed line is found by setting $T_0 = T_\infty$.

It should be noted that this conclusion does not help determining the best value for T_0 to use in Eq **12**. However, we can provide an estimate of T_0 by studying the ratio of the correlation time of the molecule τ_γ and the experimental quenching time Δt_q. A good estimate of τ_γ is given by the time constant of the exponential decay of the position autocorrelation function of an harmonically bound Brownian particle in the over–damped limit,

$$\tau_\gamma = \frac{\gamma}{M\omega^2} \quad , \qquad (2)$$

where γ is the friction coefficient of a single domain of the IgG molecule, M its mass and ω is the frequency of the harmonic oscillations. We can approximate the friction coefficient γ of a single Fab domain with that of a rigid sphere of radius $L/2$, $\gamma = 6\pi\eta_w(L/2)$. Therefore, recalling Eq. **17**, we obtain a ratio $\tau_\gamma/\Delta t_q$ of the order 10^{-4} at $T = T_{\rm amb}$ for the slowest degree of freedom (oscillations around $\phi_{\rm min}$). This means that the quenching process is significantly adiabatic. Therefore, it appears reasonable to assume as a first approximation $T_0 = T_\infty$.

Finally, as a side remark, let us shortly discuss the issue of determining the two limiting angles $\phi_{\rm min}$ and $\phi_{\rm max}$ in the distribution $\rho_1(\phi)$. By analyzing the experimental data, it is indeed reasonable to guess the existence of a potential barrier (or, alternatively, of a steep repulsive potential) around the configuration $\phi_{\rm min}$ and $\phi_{\rm max}$. Unfortunately, the statistic is at present too poor to allow for a satisfactory interpretation of the distribution $\rho_1(\phi)$ in those regions. Therefore, we chose to approximate the potential with two infinite potential barriers located at $\phi_{\rm min}$ and $\phi_{\rm max}$. This amounts to labeling as unaccessible regions that most probably are just rarely visited.